

Observation of anomalous amplitude modes in the kagome metal CsV_3Sb_5

Gan Liu,¹ Xinran Ma,¹ Kuanyu He,¹ Qing Li,¹ Hengxin Tan,² Yizhou Liu,²
Jie Xu,¹ Wenna Tang,¹ Kenji Watanabe,³ Takashi Taniguchi,⁴ Libo Gao,^{1,5}
Yaomin Dai,^{1,5} Hai-Hu Wen,^{1,5} Binghai Yan,^{2,*} and Xiaoxiang Xi^{1,5,†}

¹*National Laboratory of Solid State Microstructures and Department of Physics,
Nanjing University, Nanjing 210093, China*

²*Department of Condensed Matter Physics,
Weizmann Institute of Science, Rehovot 7610001, Israel*

³*Research Center for Functional Materials,
National Institute for Materials Science,
1-1 Namiki, Tsukuba 305-0044, Japan*

⁴*International Center for Materials Nanoarchitectonics,
National Institute for Materials Science,
1-1 Namiki, Tsukuba 305-0044, Japan*

⁵*Collaborative Innovation Center of Advanced Microstructures,
Nanjing University, Nanjing 210093, China*

* binghai.yan@weizmann.ac.il

† xxi@nju.edu.cn

Abstract

The charge-density wave (CDW) phase is often accompanied by the condensation of a soft acoustic phonon mode, giving rise to lattice distortion and charge density modulation. This picture was challenged for the recently discovered kagome metal CsV_3Sb_5 , based on the evidence of absence of soft phonons. Here we report the observation of Raman-active CDW amplitude modes in this material, which are collective excitations typically thought to emerge out of frozen soft phonons. The amplitude modes strongly hybridize with other superlattice modes, imparting them with clear temperature-dependent frequency shift and broadening, rarely seen in other known CDW materials. Both the mode mixing and the large amplitude mode frequencies suggest that the CDW exhibits the character of strong electron-phonon coupling, a regime in which acoustic phonon softening can cease to exist. The observation of amplitude modes in the absence of soft phonons highlights the unconventional nature of the CDW in CsV_3Sb_5 .

Introduction

Materials with a kagome lattice can host rich phenomena encompassing quantum magnetism [1, 2], Dirac fermions [3, 4], nontrivial topology [5–7], density waves, and superconductivity [8–10]. The recently discovered kagome metals $AV_3\text{Sb}_5$ ($A = \text{K}, \text{Rb}, \text{or Cs}$) [11, 12] offer a new platform to study the interplay of these phenomena. These compounds have Fermi levels close to Dirac points or van Hove singularities [12–14], leading to a plethora of possible intriguing ground states. Indeed, charge-density waves and superconductivity have been discovered [12, 15, 16], with ample evidence showing that both types of orders are exotic. For example, the CDW transition is accompanied possibly by a large anomalous Hall effect [17, 18], and the superconductivity features a pair-density wave state [19].

The nature of the CDW state and the mechanism for its formation have been under close scrutiny. In this work, we focus on CsV_3Sb_5 , which has a CDW transition temperature $T_{\text{CDW}} = 94 \text{ K}$ [12]. Both hard-x-ray and neutron scattering showed the lack of soft acoustic phonons [20, 21], although density functional theory (DFT) calculations found two phonon instabilities at the M and L points of the Brillouin zone [22–24]. Considering that a 2×2 modulation of the crystal lattice is well established [12, 19, 25–27], the absence of soft modes apparently breaks a pattern proven generic to many known CDW systems — a soft acoustic phonon freezes to zero frequency and triggers the formation of a distorted lattice [28]. Currently, there is still no consensus on the form of the in-plane structure and the c -axis periodicity [27, 29]. The roles of Fermi-surface nesting and electron-phonon coupling are also debated. Because the period of the 2×2 superlattice matches perfectly with the Fermiology of the van Hove singularity, it is natural to ascribe the CDW transition to Fermi surface nesting [22], supported by the appreciable partial gapping of the Fermi

surface observed experimentally [30–34]. However, the calculated electronic susceptibility lacks the expected divergence [35, 36], and the effect of electron-phonon coupling may not be dismissed [21, 36].

Because the CDW features lattice distortions, studies of the lattice degree of freedom can offer insight into the mechanism. Raman scattering is a valuable tool in this respect. In well-studied CDW systems, such as the transition metal dichalcogenides, as a soft acoustic phonon mode condenses to form a distorted lattice, new Raman-active collective excitations, known as amplitude modes, emerge, providing a direct probe of the CDW order parameter [37–39] (see Fig. 1a). Conversely, the observation of amplitude modes is typically considered as evidence for the soft mode. The temperature dependence of the amplitude modes as well as the zone-folded modes, which become Raman-active due to zone folding induced by the superlattice, can both reflect the CDW transition [40–44]. Combined with symmetry information from polarization-resolved measurements, constraints can be set on the possible CDW ground state.

Here, we report Raman scattering measurements on CsV_3Sb_5 . We observe a multitude of CDW-induced modes, whose symmetries and frequencies are in good agreement with DFT calculations for a single layer CsV_3Sb_5 under inverse Star of David distortion. The observed temperature dependence of these modes and their calculated evolutions with varying lattice distortion allow us to identify two of them as amplitude modes, emerging from the predicted soft modes, although the soft modes are elusive experimentally. In contrast to mostly independent amplitude modes and zone-folded modes in well-known CDW materials [41–43], we show that they hybridize strongly in CsV_3Sb_5 , causing spectral weight redistribution to the latter and rendering them amplitude-mode-like. The anomalous hybridization and the large values of the amplitude mode frequencies provide evidence of strong-coupling CDW, offering a possible explanation for the lack of soft acoustic modes. These results stress the importance of the lattice degree of freedom and electron-phonon coupling in the CDW formation in CsV_3Sb_5 .

Results

Raman-active modes in CsV_3Sb_5

CsV_3Sb_5 crystallizes in a hexagonal lattice with the $P6/mmm$ space group [11]. Fig. 1b shows the unit cell of its crystal structure. The V atoms form a kagome net interspersed by Sb atoms (labeled Sb1), all within the ab -plane. The V atoms are further bonded by Sb atoms above and below the kagome plane (labeled Sb2). These V_3Sb_5 slabs are separated by Cs layers, with weak coupling between them to form a quasi-two-dimensional (quasi-2D) structure. Factor group analysis yields three Raman-active phonon modes, $\Gamma_{\text{Raman}} = A_{1g} + E_{2g} + E_{1g}$. The former two can be detected when the photons are polarized in the ab -plane, satisfied by the back-scattering geometry used in our experiment. These intense

modes are marked by dashed lines in Figs. 1c, d. They involve only the Sb2 atoms, with their atomic vibrations along the c -axis and within the ab -plane for the A_{1g} and E_{2g} modes, respectively; see Fig. 1b. The E_{2g} modes are a pair of degenerate vibrations with opposite circling directions, *i.e.*, opposite chiralities (see Supplementary Note 1). These two types of symmetries can be distinguished by polarization-resolved measurements. Specifically, the A_{1g} modes can be detected in the XX and LL polarization configurations, whereas the E_{2g} modes appear in the XX, XY, and LR configurations. Here, XX and XY represent collinear and cross-linear polarization for the incident and scattered photons, and LL and LR involve circularly polarized light with left (L) and right (R) helicity. A comparison of data in all four configurations is included in Supplementary Fig. 1.

Below T_{CDW} , multiple peaks emerge, highlighted by the dotted lines in Figs. 1c, d. Their origin will be discussed in the next sections. These modes are rather weak compared to the main lattice phonons. Their disappearance at 100 K suggests a close correlation with CDW formation. In contrast, many weak peak-like structures below 100 cm^{-1} lack temperature dependence, whose origin is unclear.

Fig. 1e compares the observed Raman mode frequencies with those from DFT calculations for a single layer of CsV_3Sb_5 [22], considering two possible forms of lattice distortion, the Star of David (SD) and inverse Star of David (ISD, also referred to as tri-hexagonal) structures. Both of them show the same number of A_{1g} and E_{2g} modes, but with different ordering. Overall, the calculated ISD phonons agree much better with the experimental results, as shown in the figure and in Supplementary Tab. 1. All the five predicted A_{1g} modes and five out of the eight predicted E_{2g} modes are observed. The observed A_{1g} mode below 50 cm^{-1} is unaccounted for by our calculations. This mode was also observed by pump-probe time-resolved spectroscopy, which, when compared with calculations taking into account interlayer coupling, was assigned as a Cs-mode due to CDW modulation along the c -axis [23]. Except for this mode and the three missing E_{2g} modes due to their weak scattering cross section, the symmetry ordering of all the other modes is in exact agreement between the experiment and theory. These results suggest that the CDW ground state consists of weakly coupled layers with ISD-type distortion, but CDW modulation along the c -axis is also indispensable. Since the single-layer CsV_3Sb_5 holds the key to unraveling the CDW mechanism, we attempted creating atomically thin CsV_3Sb_5 by mechanical exfoliation. However, the loss of crystallinity impeded further investigation (Supplementary Figs. 2 and 3).

Temperature dependence of Raman modes

Figs. 2a, b show the temperature dependent Raman intensity color plot for CsV_3Sb_5 , obtained in the LL and LR configurations, respectively. The intense A_{1g} and E_{2g} main lattice modes are the most conspicuous features. Figs. 2e–g show the frequency (with the corresponding value at 200 K subtracted), linewidth (full width at half maximum), and

normalized integrated area for both modes, extracted from Lorentzian fits of the peaks. The A_{1g} frequency sharply increases below T_{CDW} , whereas the E_{2g} frequency exhibits a subtle kink across the CDW transition. This is consistent with the planar ISD lattice distortion mainly involving V atoms, forcing the Sb2 atoms to displace along the c -axis, hence affecting the out-of-plane vibration of the A_{1g} mode more effectively. The calculated phonon vibration patterns and frequencies confirm this picture (see Supplementary Fig. 4 and Supplementary Tab. 1). The CDW transition also causes a faster decrease in the linewidths below T_{CDW} . This can be understood as being due to the CDW-induced partial gapping of the Fermi surface [30–34], which reduces the electron-phonon interaction. The integrated peak intensity for both phonons increases upon warming, in line with increased thermal phonon populations. The rate of increase is faster when approaching T_{CDW} from below, and interestingly, the value saturates below approximately 50 K. The renormalization of the phonon parameters across the CDW transition evidences sizable electron-phonon coupling.

CDW-induced modes are labeled in Figs. 2a, b. Except for the A_1 mode, there appears to be two types of modes, represented by A_2 and E_3 . A_2 exhibits appreciable softening and broadening upon warming toward T_{CDW} . It is overdamped before disappearing, visualized in the color plot in Fig. 2a as the streak of signal below 100 cm^{-1} between 60–90 K. These are signatures of a CDW amplitude mode [40–44], caused by the collapse of coherent CDW order near T_{CDW} . E_3 shows a smaller change of frequency and much less broadening, more consistent with the characteristics of a zone-folded mode [41], as this type of mode arises from folding a zone-boundary phonon to the zone center, making its temperature dependence of the frequency as weak as that of normal phonons. Figs. 2c, d compare the distinct temperature dependence of these two types of modes. While A_2 broadens significantly above 40 K, E_3 maintains its linewidth and suddenly vanishes above ~ 80 K. The dramatic difference in the linewidth broadening is quantified in Fig. 2i. Fig. 2h shows the frequencies of all the observed Raman modes on the same scale. Upon warming, the CDW-induced modes (A_1 excluded) soften more dramatically than the main lattice modes. While it is tempting to assign most of them as amplitude modes because of the apparent softening behavior, we show below that they are in fact zone-folded modes, mixed with the amplitude modes to partially inherit their properties.

Nature of CDW-induced modes

Although soft acoustic phonons were not detected experimentally, our DFT results show that the formation of CDW in CsV_3Sb_5 is similar to that in other well-known systems [40–44], in the sense that a soft acoustic phonon mode at the CDW wavevector condenses and gives rise to a distorted lattice [38]. The imaginary phonon modes of pristine CsV_3Sb_5 at three M points (see Supplementary Fig. 5) transform as irreducible representation M_1^+ (A_g)

of the space group $P6/mmm$ (little co-group D_{2h}). Fig. 3a shows that after the $2 \times 2 \times 1$ CDW transition, they are folded to Γ and form triply degenerate modes. With lattice distortion, they decompose to a singlet A_{1g} mode and a doublet E_{2g} mode under the point group D_{6h} :

$$3M_1^+ \rightarrow A_{1g} \oplus E_{2g}. \quad (1)$$

As the lattice distorts from the pristine phase to the stable ISD pattern, the imaginary A_{1g} and E_{2g} modes turn real with positive frequencies, expected to be observable as two Raman-active amplitude modes. The phonon wavefunctions of the soft A_{1g} and E_{2g} modes are shown in Figs. 4a, b, dominated by vibrations of V atoms. The A_{1g} mode is fully symmetric, involving breathing-type motion for the V triangles, V hexagons, and Sb2 atoms. The E_{2g} mode involves circling motion for the atoms forming the V hexagons, while the amplitude for the Sb2 vibration is almost ten times smaller.

DFT calculations further reveal that the amplitude modes strongly hybridize with the other CDW-induced Raman modes (*i.e.* the zone-folded modes always at positive frequencies at the Γ point in Fig. 3a), rendering them amplitude-mode-like, hence their apparent temperature-dependent frequencies. Figs. 4c, d show the real space wavefunctions of all the CDW-induced modes in the $2 \times 2 \times 1$ ISD phase. A_{2-5} and E_{1-4} correspond to those in Fig. 2, and E'_{1-3} are undetected experimentally. Comparison with Figs. 4a, b shows that A_{2-5} (E_{1-4}) all resemble the A_{1g} (E_{2g}) soft mode, but the difference is also apparent. The similarity results from hybridization of phonon wavefunctions.

To quantify the mode mixing, we calculated the overlap between the soft modes and all the real modes of the stable ISD phase by projecting the phonon wavefunctions, $P_f = |\langle \mathbf{u}_f | \mathbf{u}_{SM} \rangle|^2$, where $|\mathbf{u}_{SM}\rangle$ refers to the wavefunction of the soft modes shown in Figs. 4a, b and $|\mathbf{u}_f\rangle$ refers to the wavefunction of the mode at frequency f in the ISD phase. The results in Fig. 3b show that as the soft A_{1g} and E_{2g} modes shift from negative to positive frequencies and turn into amplitude modes, they hybridize with most of the zone-folded modes belonging to the same irreducible representation. The amount of calculated projection in the stable ISD phase correlates reasonably well with the observed mode intensity in Fig. 1c, d. A_2 and E_1 are residual amplitude modes after mode mixing. E'_{1-3} show minor projection from the E_{2g} soft mode because of negligible wavefunction overlap, and accordingly their scattering cross section is weak. E_{2-4} all involve V triangles (Fig. 4d), indicating that they have contributions unrelated with the E_{2g} soft mode. Indeed, as discussed earlier, E_3 shows clear experimental signatures of a zone-folded mode.

The A_2 mode was also observed by Wulferding *et al.* in their Raman study [45] and by time-resolved pump-probe spectroscopy [23, 46]. However, in these works, it was suggested to emerge below ~ 60 K [23, 45, 46], hence ascribed to another phase transition associated with a unidirectional order [19, 25, 26]. According to our data (Fig. 2a), the A_2 mode survives above

60 K, and there is no clear evidence for two distinct phase transitions. Its vibration pattern shown in Fig. 4c confirms no relation with the unidirectional order. Another Raman study by Wu *et al.* [47] reported a similar set of modes as ours, but with different relative intensities. They also observed extra modes that are possibly due to stronger c -axis modulation in their sample.

Discussion

The anomalously large hybridization between the amplitude modes and zone-folded modes is rare, because they are mostly decoupled in the canonical CDW materials, with the amplitude modes dominating the spectral intensity [41–43]. The hybridization is highly unusual, because the A_2 and E_1 amplitude modes and the zone-folded Raman modes span a wide frequency range, and they do not overlap in energy (except for E_1 and E'_1) to exhibit the typical anti-crossing [48, 49]. Their strong coupling suggests that the hybridization occurs indirectly, through interaction with the common electronic system. As the Fermi surface instability associated with the van Hove singularity is from the V bands [22], modes mainly involving V (including A_{2-5} and E_{1-4}) naturally mix with the amplitude modes, whereas those mainly involving Sb (including E'_{1-2} and the A_{1g} and E_{2g} main lattice modes) do not. Similar mode mixing was also observed in the quasi-one-dimensional (quasi-1D) $K_{0.3}MoO_3$ using time-resolved pump-probe spectroscopy [50], and a simple model based on Ginzburg-Landau theory can well describe the entanglement of the electronic and lattice parts of the CDW order parameter. The similar phenomena observed in two systems with different dimensionality suggest the importance of electron-phonon coupling in both materials.

However, a soft acoustic phonon is well established in $K_{0.3}MoO_3$ [51], but shown to be absent in CsV_3Sb_5 [20, 21]. In the mean field weak-coupling theory [28, 38], the acoustic phonon softening, known as Kohn anomaly [52], is a direct consequence of the divergent electronic susceptibility, which screens the phonon vibration at the CDW wavevector. In reality, the singular electronic susceptibility is smeared out, especially at dimensions higher than one, and momentum dependent electron-phonon coupling dictates the phonon renormalization in certain systems such as $2H-NbSe_2$ [53, 54]. The lack of soft acoustic phonons in CsV_3Sb_5 clearly rules out both mechanisms. Instead, CsV_3Sb_5 may fall into the strong electron-phonon coupling regime [55], in which the non-detection of Kohn anomaly in the quasi-1D $(TaSe_4)_2I$, $NbSe_3$, and $BaVS_3$ has also been reported [56–58]. In all these materials, strong electron-phonon coupling tends to localize electrons, violating the adiabatic Born-Oppenheimer approximation [55] used in DFT. Failure of the conduction electrons to screen the phonon vibration can naturally explain the absence of phonon softening [59].

The strong-coupling nature of the CDW in CsV_3Sb_5 is indeed supported by multiple facts, according to the qualitative criteria discussed in Ref. [28]. The CDW-induced gap Δ_{CDW} is

large, with $2\Delta_{\text{CDW}}/k_B T_{\text{CDW}} \approx 22$ according to infrared spectroscopy [30], where k_B is the Boltzmann constant. The lattice distortion is substantial (amounting to about 5% of the lattice constant [22]), the distorted lattice exhibits clustering of V atoms to form trimers and hexamers, and the CDW locks with the pristine lattice to form a commensurate structure, all indicating local chemical bonding [22, 35]. Moreover, DFT shows that the elastic potential for the ions in the pristine structure features double minima deeper than the thermal energy $k_B T_{\text{CDW}}$ at the transition [22], a defining feature of the strong-coupling theory proposed by Gor'kov [55]. Such potential well traps the ions in one of its minima, precluding soft phonon condensation. From the perspective of Raman scattering, the electron-phonon coupling constant λ can be estimated from the amplitude mode frequency ω_{AM} and the unscreened soft mode frequency ω_{SM}^0 as $\lambda = (\omega_{\text{AM}}/\omega_{\text{SM}}^0)^2$, valid on the mean-field level [38]. The results for CsV_3Sb_5 and a variety of other CDW materials are compiled in Fig. 5. Notably, the four quasi-2D compounds $2H\text{-NbSe}_2$, $2H\text{-TaSe}_2$, CsV_3Sb_5 , and $1T\text{-TaS}_2$ are roughly located in the expected order according to their T_{CDW} , Δ_{CDW} , and commensurability. The frequencies of the amplitude modes in CsV_3Sb_5 are large, only lower than that of the higher one in $1T\text{-TiSe}_2$. Although the exact value of λ may not be meaningful beyond the weak-coupling limit, these results clearly indicate the strong-coupling nature of the CDW in CsV_3Sb_5 .

Our Raman results offer informative insights into the CDW phase in CsV_3Sb_5 , suggesting the dominance of the single layer in driving the transition and evidencing strong electron-phonon coupling. CsV_3Sb_5 represents a unique case in which the amplitude modes emerge in the absence of soft acoustic phonons. As important collective excitations of the CDW ground state, how they form without being driven by folding of a soft acoustic phonon warrants further investigation. Although DFT accurately predicts the CDW-induced Raman modes in the zero-temperature limit, in good agreement with our experiment, to understand how the amplitude modes emerge below T_{CDW} apparently requires models and computational methods working at finite temperature.

Methods

Sample preparation

CsV_3Sb_5 single crystals were synthesized using the flux method [11]. The freshly cleaved surface of the samples was used in the study of bulk crystals. Raman scattering spectroscopy was performed using home-built confocal microscopy setups in the back-scattering geometry with 532 nm laser excitation. The normally incident light was focused on the sample to a micron-sized spot, and the scattered light was directed through Bragg notch filters to access the low-wavenumber region. The Raman signal was collected using a grating spectrograph and a liquid-nitrogen-cooled charge-coupled device. The samples were mounted in a vacuum chamber during data acquisition. Temperature control was achieved using a Montana Instrument Cryostation.

Calculations

The DFT calculation results by Tan *et al.* [22] are used to compare with the experiment. Details of the calculations can be found therein. In addition, we calculated the force constants by Vienna *ab-initio* Simulation Package (VASP) [60] and computed the phonon dispersion relation by Phonopy [61]. For the DFT calculation, a $5 \times 5 \times 5$ \mathbf{k} mesh and an energy cutoff of 400 eV were used.

Data availability

The data in Figure 1e are available in Supplementary Table 1. Other data are available from the corresponding authors upon request.

References

-
- [1] Sachdev, S. Kagomé- and triangular-lattice Heisenberg antiferromagnets: Ordering from quantum fluctuations and quantum-disordered ground states with unconfined bosonic spinons. *Phys. Rev. B* **45**, 12377–12396 (1992). URL <https://link.aps.org/doi/10.1103/PhysRevB.45.12377>.
 - [2] Han, T.-H. *et al.* Fractionalized excitations in the spin-liquid state of a kagome-lattice antiferromagnet. *Nature* **492**, 406–410 (2012). URL <https://doi.org/10.1038/nature11659>.
 - [3] Mazin, I. I. *et al.* Theoretical prediction of a strongly correlated Dirac metal. *Nat. Commun.* **5**, 4261 (2014). URL <https://doi.org/10.1038/ncomms5261>.
 - [4] Ye, L. *et al.* Massive Dirac fermions in a ferromagnetic kagome metal. *Nature* **555**, 638–642 (2018). URL <https://doi.org/10.1038/nature25987>.
 - [5] Tang, E., Mei, J.-W. & Wen, X.-G. High-temperature fractional quantum Hall states. *Phys. Rev. Lett.* **106**, 236802 (2011). URL <https://link.aps.org/doi/10.1103/PhysRevLett.106.236802>.
 - [6] Xu, G., Lian, B. & Zhang, S.-C. Intrinsic quantum anomalous Hall effect in the kagome lattice $\text{Cs}_2\text{LiMn}_3\text{F}_{12}$. *Phys. Rev. Lett.* **115**, 186802 (2015). URL <https://link.aps.org/doi/10.1103/PhysRevLett.115.186802>.
 - [7] Kang, M. *et al.* Topological flat bands in frustrated kagome lattice CoSn. *Nat. Commun.* **11**, 4004 (2020). URL <https://doi.org/10.1038/s41467-020-17465-1>.
 - [8] Yu, S.-L. & Li, J.-X. Chiral superconducting phase and chiral spin-density-wave phase in a Hubbard model on the kagome lattice. *Phys. Rev. B* **85**, 144402 (2012). URL <https://link.aps.org/doi/10.1103/PhysRevB.85.144402>.
 - [9] Kiesel, M. L., Platt, C. & Thomale, R. Unconventional Fermi surface instabilities in the kagome Hubbard model. *Phys. Rev. Lett.* **110**, 126405 (2013). URL <https://link.aps.org/>

- [doi/10.1103/PhysRevLett.110.126405](https://doi.org/10.1103/PhysRevLett.110.126405).
- [10] Wang, W.-S., Li, Z.-Z., Xiang, Y.-Y. & Wang, Q.-H. Competing electronic orders on kagome lattices at van Hove filling. *Phys. Rev. B* **87**, 115135 (2013). URL <https://link.aps.org/doi/10.1103/PhysRevB.87.115135>.
- [11] Ortiz, B. R. *et al.* New kagome prototype materials: discovery of KV_3Sb_5 , RbV_3Sb_5 , and CsV_3Sb_5 . *Phys. Rev. Mater.* **3**, 094407 (2019). URL <https://link.aps.org/doi/10.1103/PhysRevMaterials.3.094407>.
- [12] Ortiz, B. R. *et al.* CsV_3Sb_5 : A \mathbb{Z}_2 Topological Kagome Metal with a Superconducting Ground State. *Phys. Rev. Lett.* **125**, 247002 (2020). URL <https://link.aps.org/doi/10.1103/PhysRevLett.125.247002>.
- [13] Liu, Z. *et al.* Charge-density-wave-induced bands renormalization and energy gaps in a kagome superconductor RbV_3Sb_5 . *Phys. Rev. X* **11**, 041010 (2021). URL <https://link.aps.org/doi/10.1103/PhysRevX.11.041010>.
- [14] Kang, M. *et al.* Twofold van Hove singularity and origin of charge order in topological kagome superconductor CsV_3Sb_5 . *Nature Physics* (2022). URL <https://doi.org/10.1038/s41567-021-01451-5>.
- [15] Ortiz, B. R. *et al.* Superconductivity in the \mathbb{Z}_2 kagome metal KV_3Sb_5 . *Phys. Rev. Mater.* **5**, 034801 (2021). URL <https://link.aps.org/doi/10.1103/PhysRevMaterials.5.034801>.
- [16] Yin, Q. *et al.* Superconductivity and normal-state properties of kagome metal RbV_3Sb_5 single crystals. *Chin. Phys. Lett.* **38**, 037403 (2021). URL <https://doi.org/10.1088/0256-307x/38/3/037403>.
- [17] Yang, S.-Y. *et al.* Giant, unconventional anomalous Hall effect in the metallic frustrated magnet candidate, KV_3Sb_5 . *Sci. Adv.* **6**, eabb6003 (2020). URL <https://advances.sciencemag.org/content/advances/6/31/eabb6003.full.pdf>.
- [18] Yu, F. H. *et al.* Concurrence of anomalous Hall effect and charge density wave in a superconducting topological kagome metal. *Phys. Rev. B* **104**, L041103 (2021). URL <https://link.aps.org/doi/10.1103/PhysRevB.104.L041103>.
- [19] Chen, H. *et al.* Roton pair density wave in a strong-coupling kagome superconductor. *Nature* **599**, 222–228 (2021). URL <https://doi.org/10.1038/s41586-021-03983-5>.
- [20] Li, H. *et al.* Observation of unconventional charge density wave without acoustic phonon anomaly in kagome superconductors AV_3Sb_5 ($A = \text{Rb}, \text{Cs}$). *Phys. Rev. X* **11**, 031050 (2021). URL <https://link.aps.org/doi/10.1103/PhysRevX.11.031050>.
- [21] Xie, Y. *et al.* Electron-phonon coupling in the charge density wave state of CsV_3Sb_5 (2021). URL <https://arxiv.org/abs/2111.00654>. 2111.00654.
- [22] Tan, H., Liu, Y., Wang, Z. & Yan, B. Charge density waves and electronic properties of superconducting kagome metals. *Phys. Rev. Lett.* **127**, 046401 (2021). URL <https://link.aps.org/doi/10.1103/PhysRevLett.127.046401>.

- [23] Ratcliff, N., Hallett, L., Ortiz, B. R., Wilson, S. D. & Harter, J. W. Coherent phonon spectroscopy and interlayer modulation of charge density wave order in the kagome metal CsV_3Sb_5 . *Phys. Rev. Mater.* **5**, L111801 (2021). URL <https://link.aps.org/doi/10.1103/PhysRevMaterials.5.L111801>.
- [24] Christensen, M. H., Birol, T., Andersen, B. M. & Fernandes, R. M. Theory of the charge density wave in $AV_3\text{Sb}_5$ kagome metals. *Phys. Rev. B* **104**, 214513 (2021). URL <https://link.aps.org/doi/10.1103/PhysRevB.104.214513>.
- [25] Zhao, H. *et al.* Cascade of correlated electron states in the kagome superconductor CsV_3Sb_5 . *Nature* **599**, 216–221 (2021). URL <https://doi.org/10.1038/s41586-021-03946-w>.
- [26] Wang, Z. *et al.* Electronic nature of chiral charge order in the kagome superconductor CsV_3Sb_5 . *Phys. Rev. B* **104**, 075148 (2021). URL <https://link.aps.org/doi/10.1103/PhysRevB.104.075148>.
- [27] Liang, Z. *et al.* Three-dimensional charge density wave and surface-dependent vortex-core states in a kagome superconductor CsV_3Sb_5 . *Phys. Rev. X* **11**, 031026 (2021). URL <https://link.aps.org/doi/10.1103/PhysRevX.11.031026>.
- [28] Rossnagel, K. On the origin of charge-density waves in select layered transition-metal dichalcogenides. *Journal of Physics: Condensed Matter* **23**, 213001 (2011). URL <https://doi.org/10.1088/0953-8984/23/21/213001>.
- [29] Ortiz, B. R. *et al.* Fermi surface mapping and the nature of charge-density-wave order in the kagome superconductor CsV_3Sb_5 . *Phys. Rev. X* **11**, 041030 (2021). URL <https://link.aps.org/doi/10.1103/PhysRevX.11.041030>.
- [30] Zhou, X. *et al.* Origin of charge density wave in the kagome metal CsV_3Sb_5 as revealed by optical spectroscopy. *Phys. Rev. B* **104**, L041101 (2021). URL <https://link.aps.org/doi/10.1103/PhysRevB.104.L041101>.
- [31] Uykur, E. *et al.* Low-energy optical properties of the nonmagnetic kagome metal CsV_3Sb_5 . *Phys. Rev. B* **104**, 045130 (2021). URL <https://link.aps.org/doi/10.1103/PhysRevB.104.045130>.
- [32] Nakayama, K. *et al.* Multiple energy scales and anisotropic energy gap in the charge-density-wave phase of the kagome superconductor CsV_3Sb_5 . *Phys. Rev. B* **104**, L161112 (2021). URL <https://link.aps.org/doi/10.1103/PhysRevB.104.L161112>.
- [33] Lou, R. *et al.* Charge-density-wave-induced peak-dip-hump structure and the multiband superconductivity in a kagome superconductor CsV_3Sb_5 . *Phys. Rev. Lett.* **128**, 036402 (2022). URL <https://link.aps.org/doi/10.1103/PhysRevLett.128.036402>.
- [34] Luo, Y. *et al.* Distinct band reconstructions in kagome superconductor CsV_3Sb_5 (2021). URL <https://arxiv.org/abs/2106.01248>. 2106.01248.
- [35] Wang, C., Liu, S., Jeon, H. & Cho, J.-H. Origin of charge density wave in the layered kagome metal CsV_3Sb_5 . *Phys. Rev. B* **105**, 045135 (2022). URL <https://link.aps.org/doi/10.1103/PhysRevB.105.045135>.

- 1103/PhysRevB.105.045135.
- [36] Ye, Z., Luo, A., Yin, J.-X., Zahid Hasan, M. & Xu, G. Structural instability and charge modulations in the Kagome superconductor AV_3Sb_5 (2021). URL <https://arxiv.org/abs/2111.07314>. 2111.07314.
- [37] Rice, M. & Strässler, S. Theory of the soft phonon mode and dielectric constant below the Peierls transition temperature. *Solid State Communications* **13**, 1931–1933 (1973). URL <https://www.sciencedirect.com/science/article/pii/0038109873900033>.
- [38] Grüner, G. *Density Waves in Solids*. Advanced book program: Addison-Wesley (Perseus Books Group, 2000).
- [39] Sugai, S. Lattice vibrations in the charge-density-wave states of layered transition metal dichalcogenides. *phys. stat. sol. (b)* **129**, 13–39 (1985). URL <http://dx.doi.org/10.1002/pssb.2221290103>.
- [40] Travaglini, G., Mörke, I. & Wachter, P. CDW evidence in one-dimensional $K_{0.3}MoO_3$ by means of Raman scattering. *Solid State Commun* **45**, 289–292 (1983). URL <https://www.sciencedirect.com/science/article/pii/0038109883904830>.
- [41] Joshi, J. *et al.* Short-range charge density wave order in $2H-TaS_2$. *Phys. Rev. B* **99**, 245144 (2019). URL <https://link.aps.org/doi/10.1103/PhysRevB.99.245144>.
- [42] Hill, H. M. *et al.* Phonon origin and lattice evolution in charge density wave states. *Phys. Rev. B* **99**, 174110 (2019). URL <https://link.aps.org/doi/10.1103/PhysRevB.99.174110>.
- [43] Lin, D. *et al.* Patterns and driving forces of dimensionality-dependent charge density waves in $2H$ -type transition metal dichalcogenides. *Nature Commun.* **11**, 2406 (2020). URL <https://doi.org/10.1038/s41467-020-15715-w>.
- [44] Barath, H. *et al.* Quantum and classical mode softening near the charge-density-wave-superconductor transition of Cu_xTiSe_2 . *Phys. Rev. Lett.* **100**, 106402 (2008). URL <https://link.aps.org/doi/10.1103/PhysRevLett.100.106402>.
- [45] Wulferding, D. *et al.* Fermi surface instabilities in electronic Raman scattering of the metallic kagome lattice CsV_3Sb_5 (2021). URL <https://arxiv.org/abs/2108.11690>. 2108.11690.
- [46] Wang, Z. X. *et al.* Unconventional charge density wave and photoinduced lattice symmetry change in the kagome metal CsV_3Sb_5 probed by time-resolved spectroscopy. *Phys. Rev. B* **104**, 165110 (2021). URL <https://link.aps.org/doi/10.1103/PhysRevB.104.165110>.
- [47] Wu, S. *et al.* Charge density wave order in kagome metal AV_3Sb_5 ($A=Cs, Rb, K$) (2022). URL <https://arxiv.org/abs/2201.05188>. 2201.05188.
- [48] Yusupov, R. V., Mertelj, T., Chu, J.-H., Fisher, I. R. & Mihailovic, D. Single-particle and collective mode couplings associated with 1- and 2-directional electronic ordering in metallic RTe_3 ($R = Ho, Dy, Tb$). *Phys. Rev. Lett.* **101**, 246402 (2008). URL <https://link.aps.org/doi/10.1103/PhysRevLett.101.246402>.
- [49] Lavagnini, M. *et al.* Raman scattering evidence for a cascade evolution of the charge-density-

- wave collective amplitude mode. *Phys. Rev. B* **81**, 081101 (2010). URL <https://link.aps.org/doi/10.1103/PhysRevB.81.081101>.
- [50] Schäfer, H., Kabanov, V. V., Beyer, M., Biljakovic, K. & Demsar, J. Disentanglement of the electronic and lattice parts of the order parameter in a 1D charge density wave system probed by femtosecond spectroscopy. *Phys. Rev. Lett.* **105**, 066402 (2010). URL <https://link.aps.org/doi/10.1103/PhysRevLett.105.066402>.
- [51] Pouget, J. P., Hennion, B., Escribe-Filippini, C. & Sato, M. Neutron-scattering investigations of the Kohn anomaly and of the phase and amplitude charge-density-wave excitations of the blue bronze $\text{K}_{0.3}\text{MoO}_3$. *Phys. Rev. B* **43**, 8421–8430 (1991). URL <https://link.aps.org/doi/10.1103/PhysRevB.43.8421>.
- [52] Kohn, W. Image of the Fermi surface in the vibration spectrum of a metal. *Phys. Rev. Lett.* **2**, 393–394 (1959). URL <https://link.aps.org/doi/10.1103/PhysRevLett.2.393>.
- [53] Johannes, M. D. & Mazin, I. I. Fermi surface nesting and the origin of charge density waves in metals. *Phys. Rev. B* **77**, 165135 (2008). URL <https://link.aps.org/doi/10.1103/PhysRevB.77.165135>.
- [54] Zhu, X., Cao, Y., Zhang, J., Plummer, E. W. & Guo, J. Classification of charge density waves based on their nature. *Proceedings of the National Academy of Sciences* **112**, 2367–2371 (2015). URL <https://www.pnas.org/content/112/8/2367>.
- [55] Gor'kov, L. P. Strong electron-lattice coupling as the mechanism behind charge density wave transformations in transition-metal dichalcogenides. *Phys. Rev. B* **85**, 165142 (2012). URL <https://link.aps.org/doi/10.1103/PhysRevB.85.165142>.
- [56] Lorenzo, J. E. *et al.* A neutron scattering study of the quasi-one-dimensional conductor $(\text{TaSe}_4)_2\text{I}$. *Journal of Physics: Condensed Matter* **10**, 5039–5068 (1998). URL <https://doi.org/10.1088/0953-8984/10/23/010>.
- [57] Requardt, H., Lorenzo, J. E., Monceau, P., Currat, R. & Krisch, M. Dynamics in the charge-density-wave system NbSe_3 using inelastic x-ray scattering with meV energy resolution. *Phys. Rev. B* **66**, 214303 (2002). URL <https://link.aps.org/doi/10.1103/PhysRevB.66.214303>.
- [58] Ilakovac, V. *et al.* Order-disorder type of Peierls instability in BaVS_3 . *Phys. Rev. B* **103**, 014306 (2021). URL <https://link.aps.org/doi/10.1103/PhysRevB.103.014306>.
- [59] Pouget, J.-P. The Peierls instability and charge density wave in one-dimensional electronic conductors. *Comptes Rendus Physique* **17**, 332–356 (2016). URL <https://www.sciencedirect.com/science/article/pii/S163107051500225X>.
- [60] Kresse, G. & Furthmüller, J. Efficient iterative schemes for *ab initio* total-energy calculations using a plane-wave basis set. *Phys. Rev. B* **54**, 11169–11186 (1996). URL <https://link.aps.org/doi/10.1103/PhysRevB.54.11169>.
- [61] Togo, A. & Tanaka, I. First principles phonon calculations in materials science. *Scr. Mater.*

- 108**, 1–5 (2015). URL <https://doi.org/10.1016/j.scriptamat.2015.07.021>.
- [62] Hu, Y., Zheng, F., Ren, X., Feng, J. & Li, Y. Charge density waves and phonon-electron coupling in ZrTe₃. *Phys. Rev. B* **91**, 144502 (2015). URL <https://link.aps.org/doi/10.1103/PhysRevB.91.144502>.
- [63] Hoesch, M., Bosak, A., Chernyshov, D., Berger, H. & Krisch, M. Giant Kohn anomaly and the phase transition in charge density wave ZrTe₃. *Phys. Rev. Lett.* **102**, 086402 (2009). URL <https://link.aps.org/doi/10.1103/PhysRevLett.102.086402>.
- [64] Maschek, M. *et al.* Wave-vector-dependent electron-phonon coupling and the charge-density-wave transition in TbTe₃. *Phys. Rev. B* **91**, 235146 (2015). URL <https://link.aps.org/doi/10.1103/PhysRevB.91.235146>.
- [65] Weber, F. *et al.* Electron-phonon coupling and the soft phonon mode in TiSe₂. *Phys. Rev. Lett.* **107**, 266401 (2011). URL <https://link.aps.org/doi/10.1103/PhysRevLett.107.266401>.
- [66] Moncton, D. E., Axe, J. D. & DiSalvo, F. J. Study of superlattice formation in 2H-NbSe₂ and 2H-TaSe₂ by neutron scattering. *Phys. Rev. Lett.* **34**, 734–737 (1975). URL <https://link.aps.org/doi/10.1103/PhysRevLett.34.734>.
- [67] Weber, F. *et al.* Extended phonon collapse and the origin of the charge-density wave in 2H-NbSe₂. *Phys. Rev. Lett.* **107**, 107403 (2011). URL <https://link.aps.org/doi/10.1103/PhysRevLett.107.107403>.
- [68] Tsang, J. C., Smith, J. E. & Shafer, M. W. Raman spectroscopy of soft modes at the charge-density-wave phase transition in 2H-NbSe₂. *Phys. Rev. Lett.* **37**, 1407–1410 (1976). URL <https://link.aps.org/doi/10.1103/PhysRevLett.37.1407>.

Acknowledgements

This work was supported by the National Key Research and Development Program of China (Grant Nos. 2018YFA0307000 and 2017YFA0303201) and the National Natural Science Foundation of China (Grant Nos. 11774151). Growth of hexagonal boron nitride crystals was supported by the Elemental Strategy Initiative conducted by the MEXT, Japan (Grant No. JPMXP0112101001), JSPS KAKENHI (Grant No. JP20H00354), and A3 Foresight by JSPS. B.Y. acknowledges the financial support by the European Research Council (ERC Consolidator Grant “NonlinearTopo”, No. 815869) and the ISF - Quantum Science and Technology (No. 1251/19).

Author information

Contributions

X.X. conceived the project. G.L., X.M., and K.H. performed the Raman experiments. Q.L., Y.D., and H.-H.W. grew the CsV₃Sb₅ crystals. K.W. and T.T. grew the h-BN crystals. G.L. and X.X. analysed the experimental data. H.T., Y.L., and B.Y. performed the DFT calculations. J.X., W.T., and L.G. performed atomic force microscopy measurements. X.X.

and B.Y. interpreted the results and co-wrote the paper, with comments from all authors.

Corresponding authors

Correspondences should be sent to Binghai Yan (binghai.yan@weizmann.ac.il) or Xiaoxiang Xi (xxi@nju.edu.cn).

Competing interests

The authors declare no competing interests.

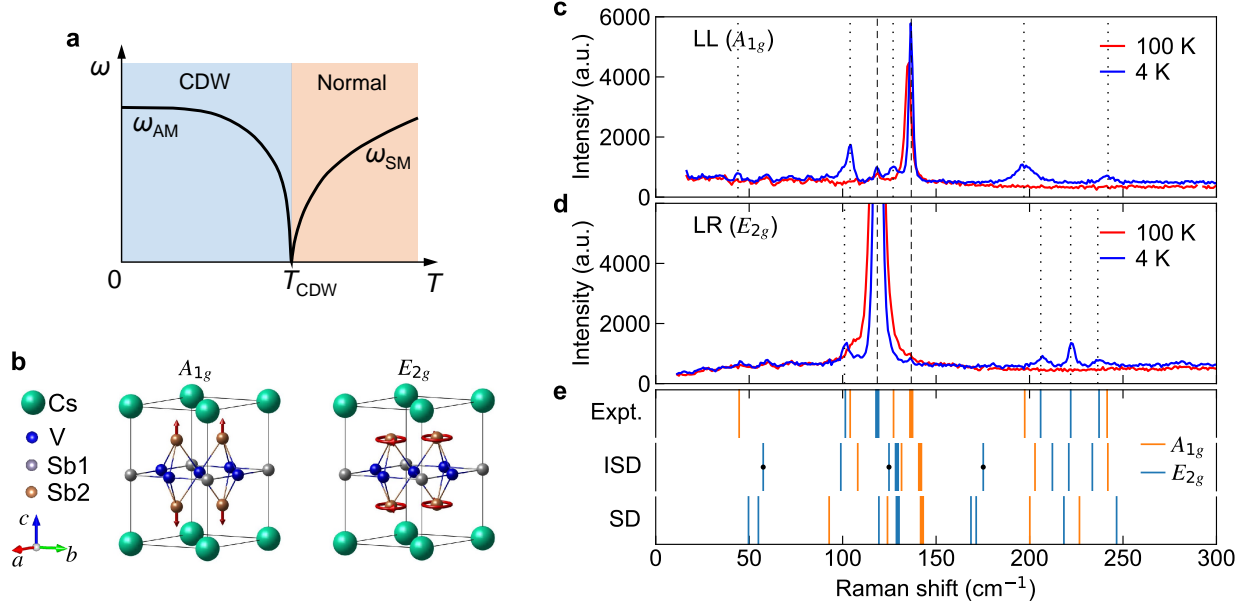


FIG. 1. **Raman-active phonon modes in CsV_3Sb_5 .** **a** Schematic illustration of the relation between the soft mode and amplitude mode in typical CDW materials, showing the latter emerges after the former freezes below T_{CDW} . **b** Crystal structure of CsV_3Sb_5 . Sb sites with different Wyckoff positions are labeled as Sb1 and Sb2. The arrows illustrate the vibration patterns of the main lattice A_{1g} and E_{2g} modes. The E_{2g} mode is doubly degenerate, and only one form is shown. **c, d** Raman spectra measured on the ab -plane at 100 K and 4 K in the LL and LR polarization configurations. The dashed lines denote the main lattice phonons, and the dotted lines indicate the CDW-induced modes. **e** Comparison of the measured (Expt.) and the calculated Raman mode frequencies for the inverse Star of David (ISD) and Star of David (SD) lattice distortions. The thick lines denote the main lattice phonons. The dots indicate modes undetected in our experiment.

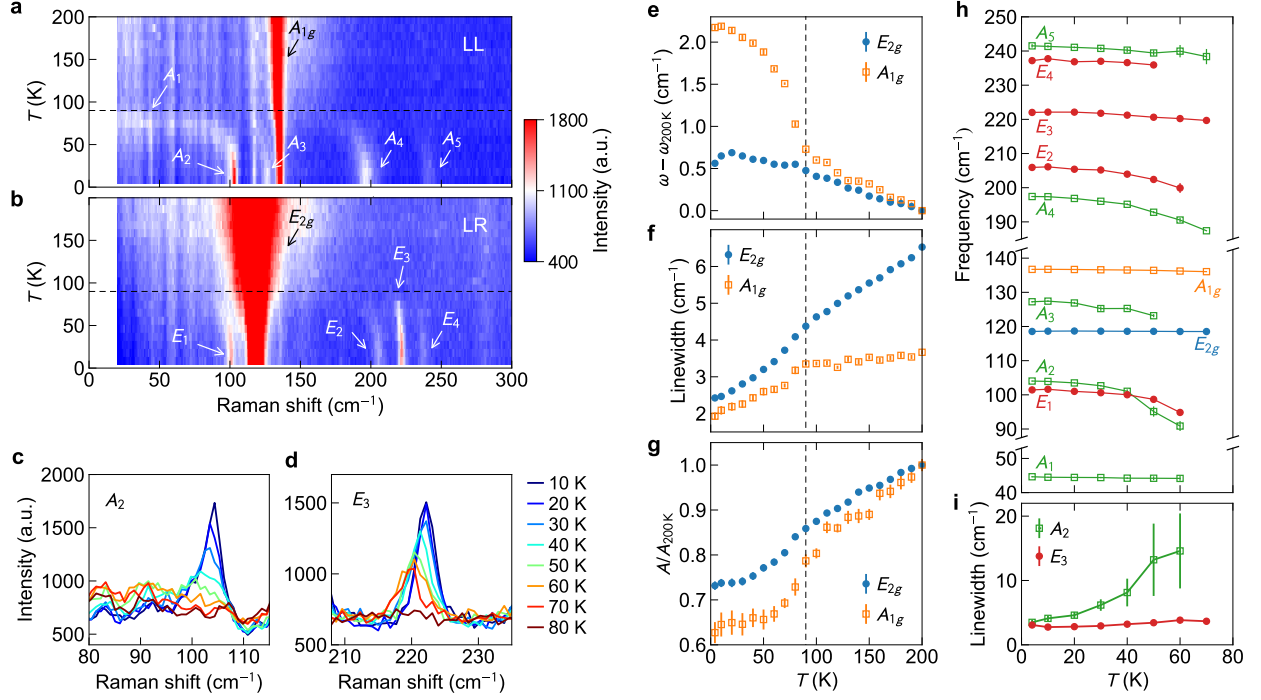


FIG. 2. **Evolution of the Raman modes in CsV_3Sb_5 across the CDW transition.** **a**, **b** Temperature-dependent Raman intensity color plot for CsV_3Sb_5 , measured in the LL and LR configurations. The normal phonon modes are labeled in black and the CDW-induced modes in white. The dashed lines mark T_{CDW} . **c**, **d** Temperature-dependent spectra for the A_2 and E_3 modes. **e–g** Frequency, linewidth, and amplitude for the E_{2g} and A_{1g} main lattice phonons. The frequency and amplitude are compared to the corresponding values at 200 K. **h** Temperature dependence of the Raman mode frequencies. **i** Temperature dependence of the linewidth of the A_2 and E_3 modes.

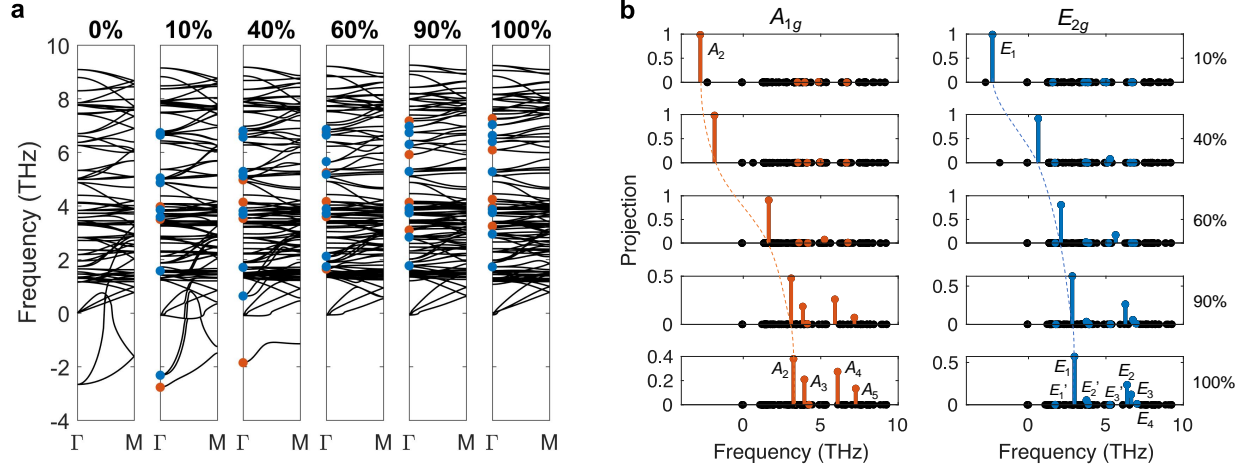


FIG. 3. Phonon band structures and mode mixing in the process of CDW distortion. a Phonon band structures. Here, 100% (0%) refers to the fully stable ISD (2×2 pristine) structure. 10% refers to the intermediate structure with 10% distortion from the pristine to ISD phases. After $2 \times 2 \times 1$ band folding with no distortion, the imaginary triply-degenerate modes form at Γ . A weak ISD-type distortion lifts the degeneracy and leads to A_{1g} and E_{2g} modes. The ISD distortion gradually transforms imaginary modes to real. **b** Projections of the imaginary A_{1g} (E_{2g}) mode with 10% distortion to all the other phonon modes at Γ , as evolving into the stable ISD phase (100%). We highlight all A_{1g} and E_{2g} modes by orange and blue dots, respectively, at the Γ point. The dashed orange (blue) curve in **b** guides eyes to show the evolution of the imaginary A_2 (E_1) modes in the CDW distortion.

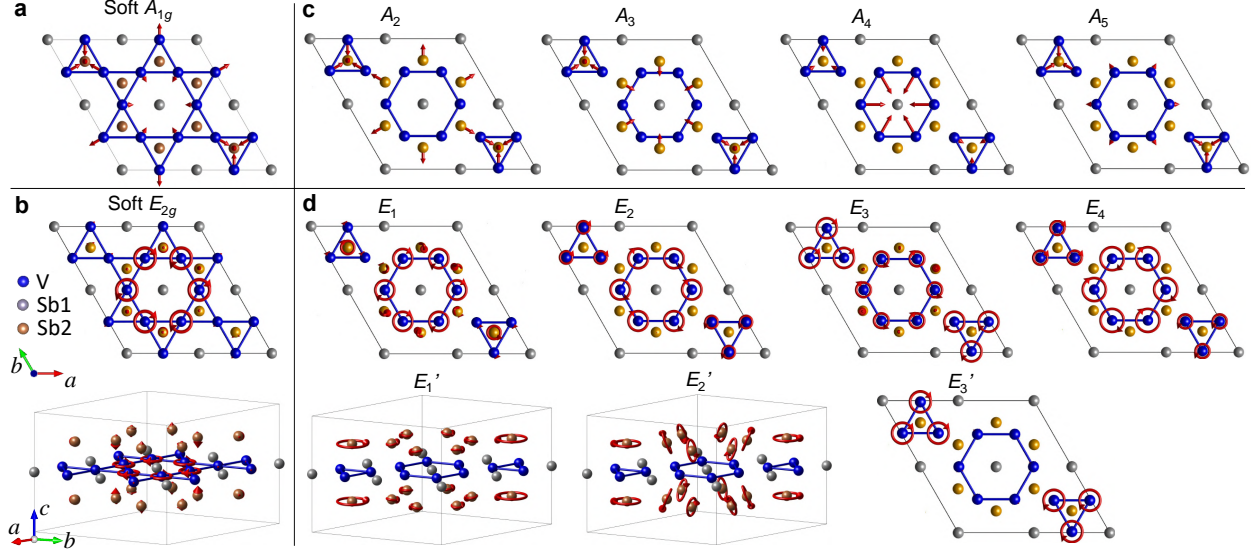


FIG. 4. Real space wavefunctions of the imaginary soft modes and the stable CDW-induced Raman modes in the $2 \times 2 \times 1$ ISD phase. **a**, **b** Soft modes with A_{1g} and E_{2g} symmetries, respectively. **c**, **d** CDW-induced A_{1g} and E_{2g} stable modes. The E_{2g} modes are pairs of chiral phonons and only one chiral mode is shown. The radius of the circles represents the amplitude of the vibration, and the arrow on the circles stands for the initial phase of the wavefunction. Cs atoms are omitted in the crystal structure for clarity, because they do not contribute to lattice vibrations.

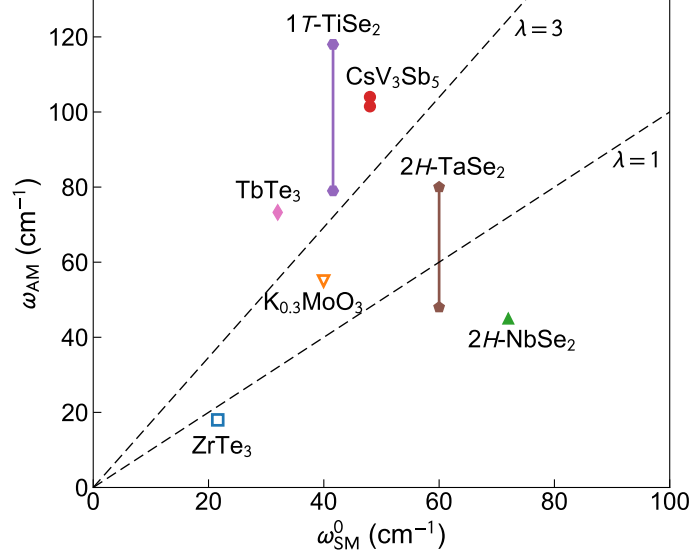


FIG. 5. **Evidence of strong-coupling CDW in CsV_3Sb_5 .** Frequency of the amplitude mode ω_{AM} in the zero-temperature limit and the unscreened frequency of the soft mode ω_{SM}^0 far above T_{CDW} for a collection of CDW materials. Some of the materials feature two amplitude modes, hence two data points connected by a vertical line. Since no soft mode is observed in CsV_3Sb_5 , ω_{SM}^0 is taken to be its acoustic phonon frequency at 300 K [21]. Open (filled) symbols indicate the material is quasi-1D (quasi-2D). The dashed lines mark electron-phonon coupling constant $\lambda = 1$ and 3 according to mean-field theory. Source of data: $ZrTe_3$ [62, 63], $TbTe_3$ [48, 64], $K_{0.3}MoO_3$ [40, 51], $1T-TiSe_2$ [44, 65], $2H-TaSe_2$ [42, 43, 66], $2H-NbSe_2$ [66–68].